IOP Publishing Smart Materials and Structures
Smart Mater. Struct. **24** (2015) 094008 (14pp) doi:10.1088/0964-1726/24/9/094008

Finite element modeling of electrically rectified piezoelectric energy harvesters

P H Wu and Y C Shu[1]

Institute of Applied Mechanics, National Taiwan University, Taipei 106, Taiwan, Republic of China

E-mail: yichung@iam.ntu.edu.tw

Received 22 January 2015, revised 24 April 2015
Accepted for publication 18 May 2015
Published 21 August 2015

Abstract

Finite element models are developed for designing electrically rectified piezoelectric energy harvesters. They account for the consideration of common interface circuits such as the standard and parallel-/series-SSHI (synchronized switch harvesting on inductor) circuits, as well as complicated structural configurations such as arrays of piezoelectric oscillators. The idea is to replace the energy harvesting circuit by the proposed equivalent load impedance together with the capacitance of negative value. As a result, the proposed framework is capable of being implemented into conventional finite element solvers for direct system-level design without resorting to circuit simulators. The validation based on COMSOL simulations carried out for various interface circuits by the comparison with the standard modal analysis model. The framework is then applied to the investigation on how harvested power is reduced due to fabrication deviations in geometric and material properties of oscillators in an array system. Remarkably, it is found that for a standard array system with strong electromechanical coupling, the drop in peak power turns out to be insignificant if the optimal load is carefully chosen. The second application is to design broadband energy harvesting by developing array systems with suitable interface circuits. The result shows that significant broadband is observed for the parallel (series) connection of oscillators endowed with the parallel-SSHI (series-SSHI) circuit technique.

Keywords: finite element modeling, piezoelectric energy harvesting, interface circuits, array of piezoelectric oscillators, equivalent load impedance

(Some figures may appear in colour only in the online journal)

1. Introduction

Significant research efforts have been made for developing vibration-based piezoelectric energy harvesting due to the ubiquitous presence of ambient vibrations as well as high electromechanical coupling in piezoelectric materials [9, 46, 55]. These include the analytic and experimental models of energy harvester structures [6, 8, 19, 37, 43, 45, 47, 50, 53, 58, 70], the search of suitable piezoelectric materials [18, 36, 41], the circuit designs for maximum power transfer [3, 12, 13, 23, 26, 27, 30, 33, 42, 49, 52, 54, 60, 62], and the advanced fabrications for creating micro-/nano-power generators [15, 24, 32, 44, 69].

However, the bottleneck for developing such techniques is that it requires the frequency matching between the resonance of a device and that of an ambient excitation source. This gives rise to the consideration of designing structures with complex configurations for frequency tuning [5, 10, 14, 17, 22, 25, 39, 40, 61]. Another approach, which has recently received significant research attentions, is to use multiple piezoelectric oscillators with slightly different resonances for enlarging bandwidth [2, 4, 11, 34, 38, 51, 56, 66, 68]. However, the increasing number of degrees of freedom of structures together with the consideration of interface circuits resulted in limited works for analyzing electrically rectified array systems [28, 29, 31, 59, 63, 64]. As a result, it raises an issue on the need for convenient numerical tools used for the system-level design of complicated configurations either in structures or circuits.

Indeed, a number of finite element techniques commonly used in engineering practice have been recently applied to the

[1] Author to whom any correspondence should be addressed.

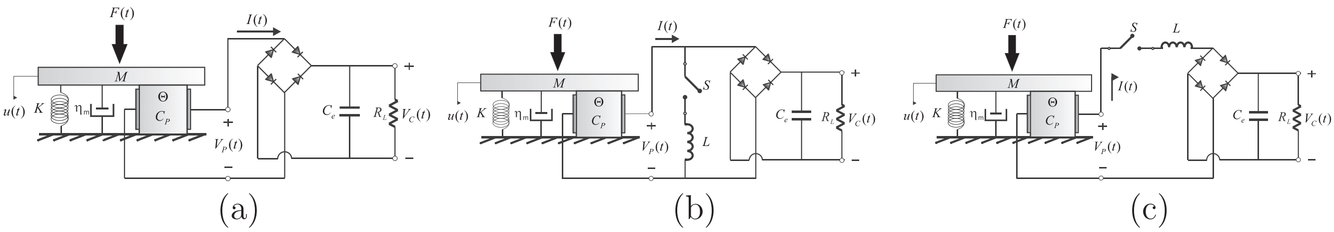

Figure 1. The parameter model of an electrically rectified piezoelectric energy harvester. The energy harvesting circuit with the standard interface as in (a), the parallel-SSHI interface as in (b), and the series-SSHI interface as in (c).

simulations of electromechanical response of a piezoelectric energy harvesting device. For example, Zhu *et al* [71] developed a coupled piezoelectric-circuit finite element model to analyze the effect of different magnitudes of load resistors on harvested power output. They used the commercial finite element solver (ANSYS) to execute simulations and proposed several design guidelines that enabled the harvesting of higher power output by varying geometric parameters of a cantilever bimorph [72]. Abdelkefi *et al* [1], Schoeftner and Buchberger [48] and Xiong and Oyadiji [65] also used ANSYS/ABAQUS to perform simulations for either model validation or parameter identification in their analytic models. Instead of using commercial finite element solvers, De Marqui *et al* [16] and Kim and Kim [21] developed finite element models suitable for plate-like/beam harvesters with moderate aspect ratios. In addition, Lumentut and Howard [35] recently presented new numerical techniques to improve the finite element model of laminated beam type. They used this model to simulate the response of a cantilevered piezoelectric energy harvester with tip mass offset.

The above mentioned works are, however, applied only to the device that is directly connected to a load resistor. This gives rise to the estimation of AC power output that an energy harvester can achieve. On the other hand, the need of DC power output limits the application of finite element method to electrically rectified piezoelectric elements. Hence, certain research efforts are made on the combination of finite element solvers and circuit simulators. But the direct combination of these two is not an easy task due to the use of nonlinear interface circuits. Hence, indirect finite element approaches by Elvin and Elvin [7] and Yang and Tang [67] were developed with the help of the SPICE software for circuit simulation. Specifically, the former approach requires transferring data between the finite element solver and SPICE simulator at each iteration and, therefore, may limit the applicability of this framework. The latter approach involves a two-step process which requires the finite element simulations to obtain the system parameters used in the circuit simulations by SPICE. This two-step approach was later improved by Kim [20] proposing an efficient identification algorithm realized as a software module. Finally, Wang *et al* [57] recently extended this two-step approach to the case of an energy harvester with two electrical output ports.

To avoid these inconveniences, a direct finite element model is developed here based on the use of equivalent load impedance proposed by Lien and Shu [28]. It suffices for the system-level design and takes into account practical energy harvesting circuits with the standard/parallel-SSHI/series-SSHI (synchronized switch harvesting on inductor) interfaces. The energy harvesting circuit is replaced by an equivalent load impedance together with the parasitic piezoelectric capacitance of negative value. As the expression of the equivalent load impedance is explicitly derived, the framework can be implemented conveniently in commercial finite element softwares without resorting to circuit simulators. In addition, the extensions to complicated structures such as array configurations are straightforward and are provided here. The proposed model is later validated by comparing it to that developed by Yang and Tang [67]. Finally, the framework is applied to the design of energy harvesting devices with ability either in power enhancement or broadband improvement by developing array configurations with suitable interface circuits.

2. Equivalent circuit models

Consider a piezoelectric oscillator connected to a rectified circuit. Under the steady-state excitation around the resonance mode, the device is commonly modeled as a mass-spring-damper-piezo-structure as illustrated in figure 1 [52, 54]. Its electromechanical response is governed by

$$M\ddot{u}(t) + \eta_m \dot{u}(t) + Ku(t) + \Theta V_p(t) = F(t), \tag{1}$$

$$-\Theta \dot{u}(t) + C_p \dot{V}_p(t) = -I(t), \tag{2}$$

where u is the displacement of the mass M, V_p is the voltage across the piezoelectric element, $F(t)$ is the applied forcing function, and η_m, K, Θ and C_p are the mechanical damping coefficient, the stiffness, the piezoelectric constant and the parasitic capacitance of the piezoelectric device. In addition, $I(t)$ is the current flowing into the specified energy harvesting circuit whose representative one is shown in figure 1(a). It consists of the standard interface including a rectifier followed by a filtering capacitance C_e for AC/DC conversion. The terminal load is presented by a resistor R_L and V_c is the DC voltage across the resistor. The rectifying bridge is assumed to be perfect here and C_e is large enough to maintain constant DC voltage V_c across R_L. Another common interface circuit used as an impedance modifier for enhancing electromechanical response is the SSHI circuit. It consists of adding up a switching device (an inductor L in series with a switch) in parallel (series) with the piezoelectric harvester structure, as

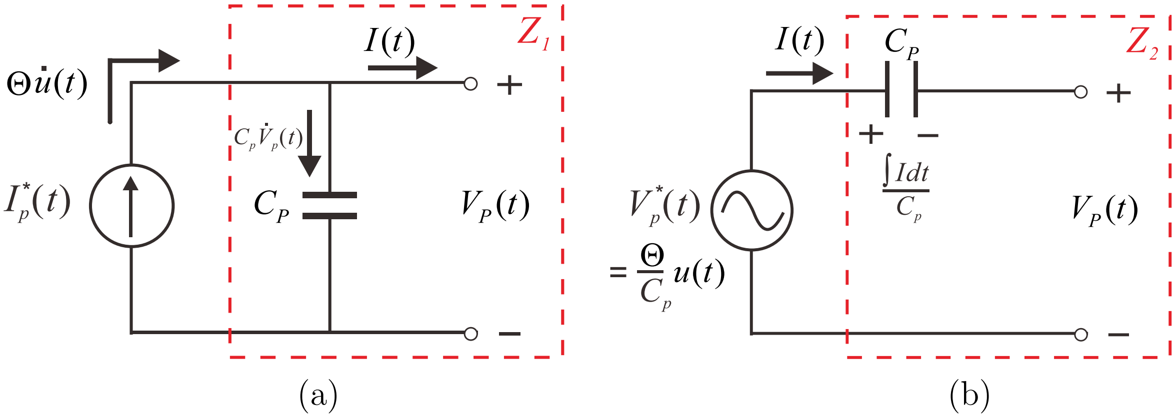

Figure 2. The schematic interpretation of an equivalent current model (a) and an equivalent voltage model (b).

also shown in figure 1(b) for parallel-SSHI, and in figure 1(c) for series-SSHI. The details on how the SSHI interface circuits work can be found in [3, 12, 30, 54]. Finally, equation (2) can be realized from the electrical perspective and is explained next.

2.1. Equivalent current model

Introducing the equivalent velocity current $I_p^*(t)$ by

$$I_p^*(t) = \Theta \dot{u}(t), \tag{3}$$

equation (2) can be rewritten as

$$I_p^*(t) = C_p \dot{V}_p(t) + I(t). \tag{4}$$

From Kirchhoff's current law, the relation between the equivalent velocity current $I_p^*(t)$ and the real current $I(t)$ is schematically demonstrated by figure 2(a).

Next, let Z_1 be the equivalent impedance of the circuit elements consisting of the piezoelectric capacitance C_p in parallel with the energy harvesting circuit, as also illustrated by the red rectangle in figure 2(a). Therefore, the voltage V_p across Z_1 is related to the current I_p^* by

$$V_p = I_p^* \cdot Z_1. \tag{5}$$

Suppose the base excitation is harmonic with a single signal, the forcing function can be presented by $F(t) = F_0 e^{jwt}$, where F_0 is the real magnitude, w is the angular frequency and $j^2 = -1$. The steady-state solution can be realized by setting [28]

$$u(t) = \bar{u} e^{jwt}, \quad V_p(t) = \bar{V}_p e^{jwt}, \tag{6}$$

where $\bar{u}$ and $\bar{V}_p$ are the complex magnitudes of displacement and piezoelectric voltage, and from equations (3) and (5), are related by

$$\bar{V}_p = \left(jw\Theta Z_1\right)\bar{u}. \tag{7}$$

Therefore, the substitution of equation (6) with the help of equation (7) into equation (1) gives the magnitude of displacement in terms of Z_1 by

$$|\bar{u}| = \frac{F_0}{\left\{\left(K - w^2 M - w\Theta^2 Z_{1\mathrm{I}}\right)^2 + \left(w\eta_m + w\Theta^2 Z_{1\mathrm{R}}\right)^2\right\}^{\frac{1}{2}}}. \tag{8}$$

Above $Z_{1\mathrm{R}}$ and $Z_{1\mathrm{I}}$ are the real and imaginary parts of the complex impedance Z_1 defined by

$$Z_1 = Z_{1\mathrm{R}} + jZ_{1\mathrm{I}}. \tag{9}$$

However, the expression of complex impedance Z_1 is still not yet decided. Fortunately, the magnitude of displacement $|\bar{u}|$ has been explicitly provided by equation (28) in [52] for the standard interface, by equation (19) in [54] for the parallel-SSHI interface, and by equation (19) in [30] for the series-SSHI interface. Thus, the comparison between equation (8) and the existing formulas gives the equivalent impedance Z_1 by

$$Z_{1\mathrm{R}}^{\mathrm{Standard}} = \frac{2R_L}{\left(\frac{\pi}{2} + C_p w R_L\right)^2},$$
$$Z_{1\mathrm{I}}^{\mathrm{Standard}} = -\frac{R_L}{\left(\frac{\pi}{2} + C_p w R_L\right)} \tag{10}$$

for the standard interface circuit,

$$Z_{1\mathrm{R}}^{\mathrm{P-SSHI}} = \frac{2R_L\left[1 + \frac{\left(1 - q_I^2\right)}{2\pi} C_p w R_L\right]}{\left(\frac{\pi}{2} + \frac{\left(1 - q_I\right)}{2} C_p w R_L\right)^2},$$
$$Z_{1\mathrm{I}}^{\mathrm{P-SSHI}} = -\frac{\frac{\left(1 - q_I\right)}{2} R_L}{\left(\frac{\pi}{2} + \frac{\left(1 - q_I\right)}{2} C_p w R_L\right)} \tag{11}$$

for the parallel-SSHI interface circuit,

$$Z_{1R}^{S-SSHI} = \frac{\dfrac{2}{C_p w}}{\dfrac{\pi}{2}\left(\dfrac{1-q_I}{1+q_I}\right) + C_p w R_L},$$
$$Z_{1I}^{S-SSHI} = -\frac{1}{C_p w} \tag{12}$$

for the series-SSHI interface circuit [28]. Above $q_I = e^{-\frac{\pi}{2Q_I}}$ and Q_I is the electric quality factor introduced in the SSHI circuits [12, 30, 54]. It is used for measuring the extent of energy loss from the inductor in series with the switch.

Finally, notice that the current flowing into the equivalent impedance Z_1 is not the real current $I(t)$. It is the equivalent velocity current $I_p^*(t)$ as also illustrated in figure 2(a). Its magnitude $\left|\bar{I}_p^*\right|$ related with the DC voltage V_c can be obtained by integrating the equation of charge balance in equation (4) over the semi-period of oscillation. This gives

$$V_c^{\text{Standard}} = \left(\frac{R_L}{\dfrac{\pi}{2} + C_p w R_L}\right)\left|\bar{I}_p^*\right|, \tag{13}$$

$$V_c^{P-SSHI} = \left(\frac{R_L}{\dfrac{\pi}{2} + \left(\dfrac{1-q_I}{2}\right) C_p w R_L}\right)\left|\bar{I}_p^*\right|, \tag{14}$$

$$V_c^{S-SSHI} = \left(\frac{R_L}{\dfrac{\pi}{2}\left(\dfrac{1-q_I}{1+q_I}\right) + C_p w R_L}\right)\left|\bar{I}_p^*\right|, \tag{15}$$

for the cases of standard, parallel-SSHI and series-SSHI circuits (see equations (7), (12) and (13) in [52, 54] and [30], respectively). The harvested average power P_h is then evaluated once the DC voltage V_c is known. It is

$$P_h = \frac{V_c^2}{R_L}. \tag{16}$$

Later in section 3.1 it will be shown that this equivalent current model can be extended to the case of parallel connection of piezoelectric oscillators, since both velocity current $I_p^*(t)$ and real current $I(t)$ are the sum of each individual one, as demonstrated in figure 5.

2.2. Equivalent voltage model

The previous equivalent current model can also be revisited by introducing the equivalent displacement voltage V_p^* by

$$V_p^*(t) = \frac{\Theta}{C_p} u(t) \quad \text{or} \quad \dot{V}_p^*(t) = \frac{\Theta}{C_p}\dot{u}(t). \tag{17}$$

Thus, equation (2) can be rewritten as

$$-\dot{V}_p^* + \dot{V}_p(t) = -\frac{1}{C_p} I(t) \quad \text{or} \quad V_p^* - \frac{1}{C_p}\int I \mathrm{d}t = V_p. \tag{18}$$

The relation between the equivalent displacement voltage V_p^* and the piezoelectric voltage V_p is schematically illustrated by figure 2(b).

Next, let Z_2 be the equivalent impedance of the circuit elements consisting of the piezoelectric capacitance C_p in series with the specified energy harvesting circuit, as also illustrated by the red rectangle in figure 2(b). Thus, from Ohm's circuit law,

$$V_p^* = I \cdot Z_2. \tag{19}$$

Under the steady-state operation, the complex magnitudes of $\bar{u}$ and $\bar{V}_p$ in equation (6) are, from the consideration of equations (17)–(19) , related by

$$\bar{V}_p = \frac{\Theta}{C_p}\bar{u} + j\frac{\Theta}{w C_p^2 Z_2}\bar{u}. \tag{20}$$

Now substituting equation (6) with equation (20) into equation (1) gives the magnitude of displacement by

$$|\bar{u}| = (F_0)\Big/ \left(\left\{\left(K - w^2 M + \frac{\Theta^2}{C_p} + \frac{\Theta^2}{C_p^2 w} Y_{2I}\right)^2 + \left(w\eta_m + \frac{\Theta^2}{C_p^2 w} Y_{2R}\right)^2\right\}^{\frac{1}{2}}\right). \tag{21}$$

Above Y_{2R} and $-Y_{2I}$ are the real and imaginary parts of the complex impedance $\dfrac{1}{Z_2}$ by

$$Y_2 = \frac{1}{Z_2} = Y_{2R} - jY_{2I}, \quad Y_{2R} = \mathrm{Re}\left\{\frac{1}{Z_2}\right\},$$
$$-Y_{2I} = \mathrm{Im}\left\{\frac{1}{Z_2}\right\}. \tag{22}$$

Again, the complex impedance Z_2 can not be determined without the explicit expression of displacement magnitude in terms of the system parameters. Using the arguments similar to deriving the equivalent impedance Z_1, Z_2 can be provided by comparing equation (21) with equation (28) in [52] for the standard interface, equation (19) in [54] for the parallel-SSHI interface, and equation (19) in [30] for the series-SSHI interface. This gives

$$Y_{2R}^{\text{Standard}} = \frac{2C_p^2 w^2 R_L}{\left(\dfrac{\pi}{2} + C_p w R_L\right)^2},$$
$$Y_{2I}^{\text{Standard}} = -\frac{\dfrac{\pi}{2} C_p w}{\left(\dfrac{\pi}{2} + C_p w R_L\right)} \tag{23}$$

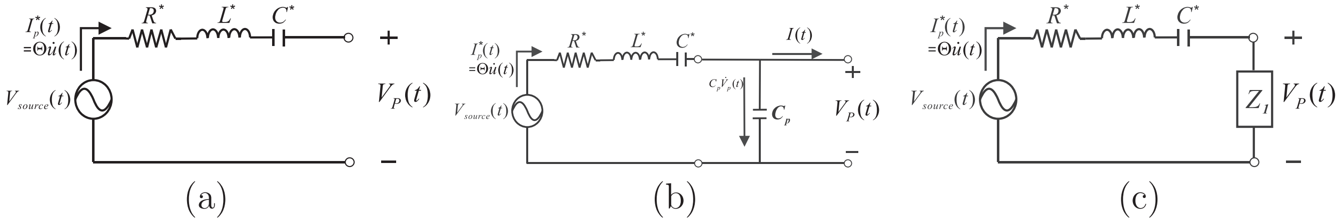

Figure 3. (a) The circuit model describes the dynamic response of a piezoelectric oscillator. (b) The circuit model stands for the electromechanical response of a piezoelectric oscillator. (c) The equivalent circuit model of the current type represents an electrically rectified piezoelectric energy harvesting system.

for the standard interface circuit,

$$Y_{2R}^{\text{P-SSHI}} = \frac{2C_p^2 w^2 R_L \left[1 + \frac{\left(1 - q_I^2\right)}{2\pi} C_p w R_L\right]}{\left(\frac{\pi}{2} + \frac{\left(1 - q_I\right)}{2} C_p w R_L\right)^2},$$
$$Y_{2I}^{\text{P-SSHI}} = -\frac{\frac{\pi}{2} C_p w}{\left(\frac{\pi}{2} + \frac{\left(1 - q_I\right)}{2} C_p w R_L\right)} \tag{24}$$

for the parallel-SSHI interface circuit,

$$Y_{2R}^{\text{S-SSHI}} = \frac{2C_p w}{\frac{\pi}{2}\left(\frac{1 - q_I}{1 + q_I}\right) + C_p w R_L},$$
$$Y_{2I}^{\text{S-SSHI}} = 0 \tag{25}$$

for the series-SSHI interface circuit [31].

Finally, the voltage across the equivalent impedance Z_2 is not the real piezoelectric voltage $V_p(t)$. Instead, it is the equivalent displacement voltage $V_p^*(t)$ as also demonstrated in figure 2(b). Its magnitude $\left|\bar{V}_p^*\right|$ can be related with the DC voltage V_c by integrating the balance of charge conservation as in equation (18) over the semi-period of oscillation. This gives

$$V_c^{\text{Standard}} = \left(\frac{C_p w R_L}{\frac{\pi}{2} + C_p w R_L}\right) \left|\bar{V}_p^*\right|, \tag{26}$$

$$V_c^{\text{P-SSHI}} = \left(\frac{C_p w R_L}{\frac{\pi}{2} + \left(\frac{1 - q_I}{2}\right) C_p w R_L}\right) \left|\bar{V}_p^*\right|, \tag{27}$$

$$V_c^{\text{S-SSHI}} = \left(\frac{C_p w R_L}{\frac{\pi}{2}\left(\frac{1 - q_I}{1 + q_I}\right) + C_p w R_L}\right) \left|\bar{V}_p^*\right|, \tag{28}$$

for the cases of standard, parallel-SSHI and series-SSHI circuits (see equations (7), (12) and (13) in [52, 54] and [30], respectively). The harvested average power P_h is therefore evaluated by equation (16) once the magnitude of displacement voltage $V_p^*(t)$ across Z_2 is determined.

Later in section 3.2 it will be shown that this equivalent voltage model can be extended to the case of series connection of piezoelectric oscillators, since both displacement voltage $V_p^*(t)$ and piezoelectric voltage $V_p(t)$ are the sum of each individual one, as demonstrated in figure 8.

3. Finite element models

The idea based on the use of the equivalent load impedance introduced in the previous section is applied to the finite element modeling of rectified piezoelectric energy harvesters. Two types of models are developed as below: one is the current type based on the use of impedance Z_1, and the other is the voltage type based on the use of impedance Z_2.

3.1. Type I model: equivalent current approach

Introducing

$$R^* = \frac{\eta_m}{\Theta^2},\ L^* = \frac{M}{\Theta^2},\ C^* = \frac{\Theta^2}{K},\quad V_{\text{source}} = \frac{F}{\Theta} \tag{29}$$

as an equivalent resistance, an equivalent inductance, an equivalent capacitance, and an equivalent voltage source. From the definition of $I_p^*(t)$ as in equation (3), equation (1) can be presented in terms of I_p^* by

$$V_p = V_{\text{source}} - L^* \frac{dI_p^*}{dt} - R^* I_p^* - \frac{1}{C^*} \int I_p^* \mathrm{d}t.$$

Its schematic interpretation based on Kirchhoff's voltage law is shown in figure 3(a). Thus, the combination of the equivalent current model presented in figure 2(a) gives the equivalent circuit model of a piezoelectric oscillator, as shown in figure 3(b).

Next, as explained in section 2.1, the impedance of the piezoelectric capacitance in parallel with the backward energy harvesting circuit is presented by Z_1, as shown by the red rectangle in figure 2(a). Therefore, figure 3(b) can be replaced with figure 3(c) which provides a full description of the equivalent circuit model for a piezoelectric energy harvesting

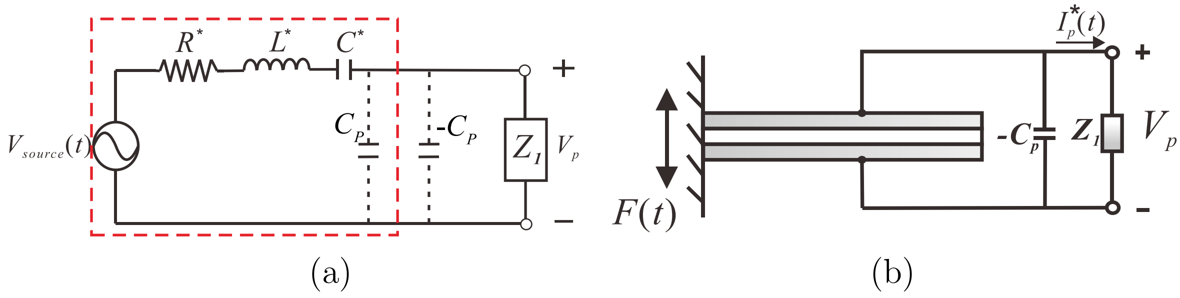

Figure 4. (a) is equivalent to the one in figure 3(c). (b) is the finite element model of the current type for the case of a single piezoelectric oscillator.

system. Notice that figure 3(c) is equivalent to figure 4(a) whose red rectangle stands for a piezoelectric oscillator as explained by figure 3(b). Hence, figure 4(a) can be interpreted as an energy harvester attached to a negative piezoelectric capacitance $(-C_p)$ in parallel with an equivalent load impedance Z_1. This gives the proposed finite element model of the current type schematically described by figure 4(b). The electromechanical frequency response around the first mode can be simulated using the harmonic analysis by finite element solvers. But note that the current flowing into the impedance Z_1 is not the real piezoelectric current $I(t)$. From figure 4(b), it is the the equivalent velocity current $I_p^*(t)$ defined by equation (3) whose magnitude is related to the DC output voltage V_c by equations (13)–(15) for the standard, parallel-SSHI and series-SSHI interfaces, respectively. Thus, at the post-processing stage, it needs the evaluation of the magnitude of I_p^* to obtain V_c, which in turn gives the harvested average power from equation (16).

The proposed finite element model offers several advantages. First from the model itself, it is simply enough to be implemented in many more commercial finite element solvers without resorting to circuit solvers. Second, it mimics the electromechanical response of a rectified piezoelectric oscillator excited harmonically. The equivalent load impedance Z_1 is explicitly provided by equations (10)–(12) for the standard, parallel-SSHI and series-SSHI interfaces.

Thus, the proposed approach provides a convenient tool for performance evaluation of a practical energy harvester device. Design guidelines can be drawn from simulations prior to assembling and testing. Finally, another advantage of the proposed model is the easy extension to the case multiple piezoelectric oscillators, as described below.

Consider an array of piezoelectric oscillators connected in parallel as shown in figure 5(a), where each subscript i refers to the ith oscillator and n is the total number of oscillators. Thus, the equivalent current model of a single oscillator described by equation (4) is extended to

$$I_p^*(t) = C_p^*\dot{V}_p(t) + I(t), \tag{30}$$

where

$$I_p^*(t) = \sum_{i=1}^{n} I_{p_i}^*(t),\ I_{p_i}^*(t) = \Theta_i \dot{u}_i(t),$$
$$C_p^* = \sum_{i=1}^{n} C_{p_i},\ I(t) = \sum_{i=1}^{n} I_i(t). \tag{31}$$

Above, $I_{p_i}^*(t)$ is interpreted as the equivalent velocity current of the ith oscillator, $I_p^*(t)$ is the overall equivalent velocity current, and C_p^* is the overall piezoelectric capacitance. Due to the type of parallel connection of oscillators, the piezoelectric voltage of each oscillator is identical $(V_{p_1} = V_{p_2} = \cdots = V_{p_n} = V_p)$ and the overall current $I(t)$ is the sum of individual current $I_i(t)$ of each oscillator. The schematic interpretation of equation (30) is illustrated by figures 5(b) and (c).

Let the red rectangle shown in figure 5(c) represent the elements including the overall piezoelectric capacitance C_p^* in parallel with the backward energy harvesting circuit. Its equivalent load impedance can be shown to be exactly identical to Z_1 as long as the piezoelectric capacitance is replaced by the overall capacitance C_p^* in equations (10)–(12) [28]. Therefore, following the arguments similar to the case of a single oscillator, figure 6 describes the finite element model of the current type for the parallel connection of multiple piezoelectric oscillators. The inclusion of the negative piezoelectric capacitance $(-C_p^*)$ is necessary, since from figure 5(c) the composition of Z_1 incorporates the impedance of C_p^*. The magnitude of the overall velocity current $I_p^*(t)$ can be determined by the harmonic analysis of finite element solvers. Thus, at the post-processing stage, the DC output voltage V_c is evaluated by equations (13)–(15) for various interfaces as long as C_p is replaced by C_p^*.

3.2. Type II model: equivalent voltage approach

The finite element model can also be developed based on the equivalent voltage approach introduced in section 2.2. Later, we will show that this approach is essential for the extension to the case of series connection of piezoelectric oscillators.

Firstly, figure 7(a) is the combination of figure 3(b) and the voltage model presented by figure 2(b). It describes a full description of a rectified piezoelectric energy harvesting system with Z_2 as the equivalent load impedance. In addition, the red rectangle shown in figure 7(a) stands for a

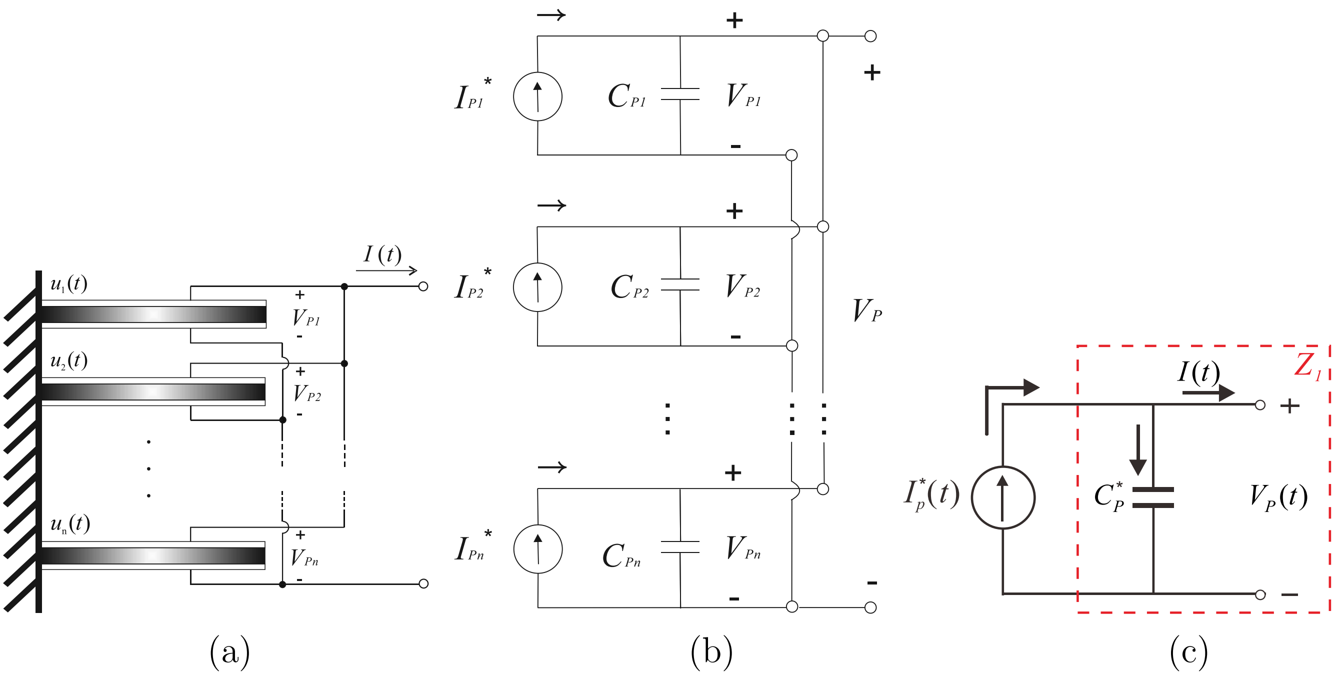

Figure 5. (a) An array of piezoelectric oscillators connected in parallel. (b) The equivalent current model of parallel connection of piezoelectric oscillators. (c) The overall equivalent current model of parallel connection of piezoelectric oscillators.

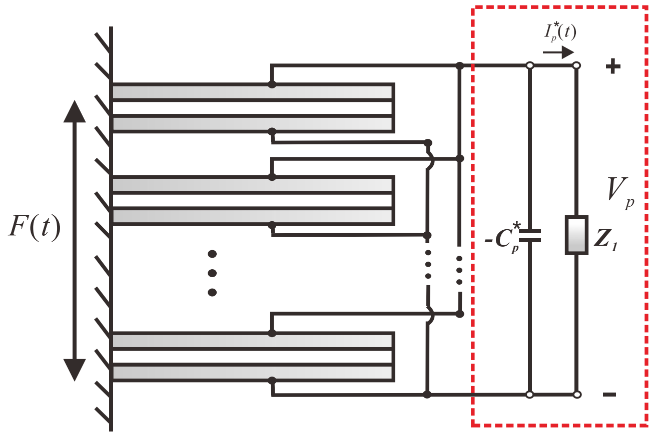

Figure 6. The schematic interpretation of the finite element model of the current type for the parallel connection of piezoelectric oscillators.

piezoelectric oscillator as illustrated in figure 3(b). Thus, figure 7(a) can be explained as an energy harvester attached to a negative piezoelectric capacitance ($-C_p$) in series with an equivalent load impedance Z_2. This gives the proposed finite element model of the voltage type and is schematically described by figure 7(b). Next, the impedance Z_2 is explicitly provided by equations (23)–(25) for the standard, parallel-SSHI and series-SSHI interfaces. Hence, there is no difficulty for implementing the proposed finite element model into commercial finite element solvers. But different from the previous type I model, the voltage across the impedance Z_2 is not the real piezoelectric voltage V_p. It is the equivalent displacement voltage $V_p^*(t)$ defined by equation (17). Its magnitude can be computed by the harmonic analysis of finite element solvers and is related to the DC output voltage V_c by equations (26)–(28) for various interface circuits. Therefore, the evaluation of DC harvested average power by equation (16) can be carried out at the post-processing stage of finite element simulations. Finally, the introduction of type II model is mainly for the extension to the case of series connection of piezoelectric oscillators, as described below.

Consider an array of piezoelectric oscillators connected in series, as shown in figure 8(a) where each subscript i refers to the ith oscillator and n is the total number of oscillators. The equivalent voltage model introduced by equation (18) is replaced by

$$V_p^* - \frac{1}{C_p^*}\int I \mathrm{d}t = V_p, \tag{32}$$

where

$$V_p^*(t) = \sum_{i=1}^{n} V_{p_i}^*(t), \quad V_{p_i}^*(t) = \frac{\Theta_i}{C_{p_i}} u_i(t),$$
$$\frac{1}{C_p^*} = \sum_{i=1}^{n} \frac{1}{C_{p_i}}, \quad V_p(t) = \sum_{i=1}^{n} V_{p_i}(t). \tag{33}$$

Above $V_{p_i}^*(t)$ is interpreted as the equivalent displacement voltage of the ith oscillator, $V_p^*(t)$ is the overall equivalent displacement voltage, and C_p^* is the overall piezoelectric capacitance. The series connection of oscillators guarantees $I(t) = I_1 = I_2 = \cdots = I_n$ and the overall piezoelectric voltage $V_p(t)$ is the sum of the individual voltage $V_{p_i}(t)$ of each oscillator. The schematic interpretation of equation (32) is provided by figures 8(b) and (c).

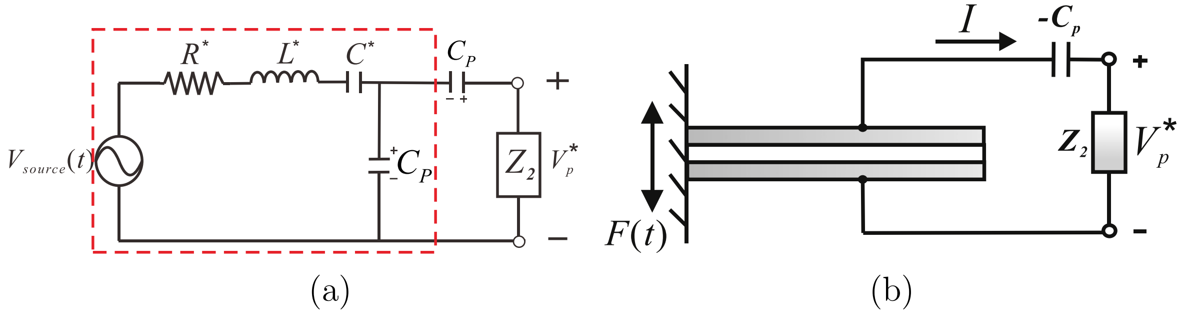

Figure 7. (a) The equivalent circuit model of the voltage type represents an electrically rectified piezoelectric energy harvesting system. (b) The finite element model of the voltage type for the case of a single piezoelectric oscillator.

The red rectangle shown in figure 8(c) consists of circuit elements including the overall piezoelectric capacitance C_p^* in series with the backward energy harvesting circuit. It can be shown that its equivalent load impedance is also exactly identical to Z_2 whenever the energy harvesting circuits shown in figure 1 are considered [31]. However, the piezoelectric capacitance has to be replaced by C_p^* in the expression of Z_2 in equations (23)–(25) for various interface circuits. Therefore, following the arguments similar to the case of a single oscillator, the finite element model of the voltage type is schematically presented by figure 9 for the series connection of piezoelectric oscillators. Once again, the inclusion of the negative piezoelectric capacitance $(-C_p^*)$ is necessary for avoiding repetition since Z_2 incorporates the impedance of C_p^* from figure 8(c). Finally, under the harmonic analysis from the standard finite element solver, the overall displacement voltage $V_p^*(t)$ across the load impedance Z_2 can be computed. Thus, at the post-processing stage, the DC output voltage V_c across the external load R_L is then obtained by recalling equations (26)–(28) for the standard/parallel-SSHI/series-SSHI interface circuits. Again, C_p has to be replaced by C_p^* in these formulations.

4. Results

4.1. Validation

The validation of the proposed approach is carried out numerically by comparing it to the two-step finite element model proposed by Yang and Tang [67]. Their approach first carries out finite element simulations to identify the equivalent system parameters required for the equivalent circuit model as in equations (1) and (2). The electric response is then simulated based on the standard SPICE circuit solver. Instead, our approach provides direct finite element simulations without circuit solvers.

Consider a model example that is a piezoelectric cantilever bimorph consisting of a Cu substrate with two piezoelectric patches made of PZT-5H on the top and bottom surfaces. The geometric properties of the cantilever bimorph are given by table 1 and the material parameters of Cu and PZT-5H are chosen from the standard data base installed in the commercial COMSOL software, as listed in table 2. The device is excited harmonically with the level of the base acceleration at 2 m s^{-2}. The loss factor is set to be 0.014 and the inversion quality factor is chosen to be $q_I = 0.6$ for the SSHI interfaces. For comparisons, table 3 lists the equivalent parameters identified by the simulations of Yang and Tang's finite element approach [67].

The commercial finite element solver COMSOL is employed and around 2600 triangular elements with Lagrange-Quadratic type are used for simulation.

The electric response of the device attached to the standard/parallel-SSHI/series-SSHI interfaces is shown in figure 10 where harvested power is against frequency for various resistive loads. The results based on the Yang and Tang's two-step finite element model are presented by various continuous lines of different colors, while the simulations based on the present model of the current and voltage types are marked by ◯ and X, respectively. It is obvious to see that the agreement among these simulation results is excellent, confirming the accuracy of the proposed finite element model.

Two remarks are made from the simulation results shown in figure 10 and will be further discussed in the next section. First, from table 3, the ratio of electromechanical coupling factor $(k_e^2 = \frac{\Theta^2}{KC_p})$ to the mechanical damping ratio $(\zeta_m = \frac{\eta_m}{2\sqrt{KM}})$ is $\frac{k_e^2}{\zeta_m} > 10$. It is in the range of strong electromechanical coupling, giving rise to two identical peaks of optimal harvested power in the case of the standard interface [52], as illustrated in figure 10(a). The first optimal power occurs at a frequency close to the short circuit resonance with small load resistance as presented by the blue curve, while the second optimal power appears at around the open circuit resonance with large load resistance as presented by the red curve. The next observation is about the relation between the system using the standard interface and that using the SSHI interface. Indeed, the optimal response of a parallel-SSHI system is similar to that based on the use of standard interface and operated at the short circuit resonance [54] (see the comparison between two blue curves in figures 10(a) and (b)). On the other hand, the optimal response of a series-SSHI system is similar to that based on the use of standard interface and operated at the open circuit resonance [30] (see the comparison between two red curves in figures 10(a) and (c)).

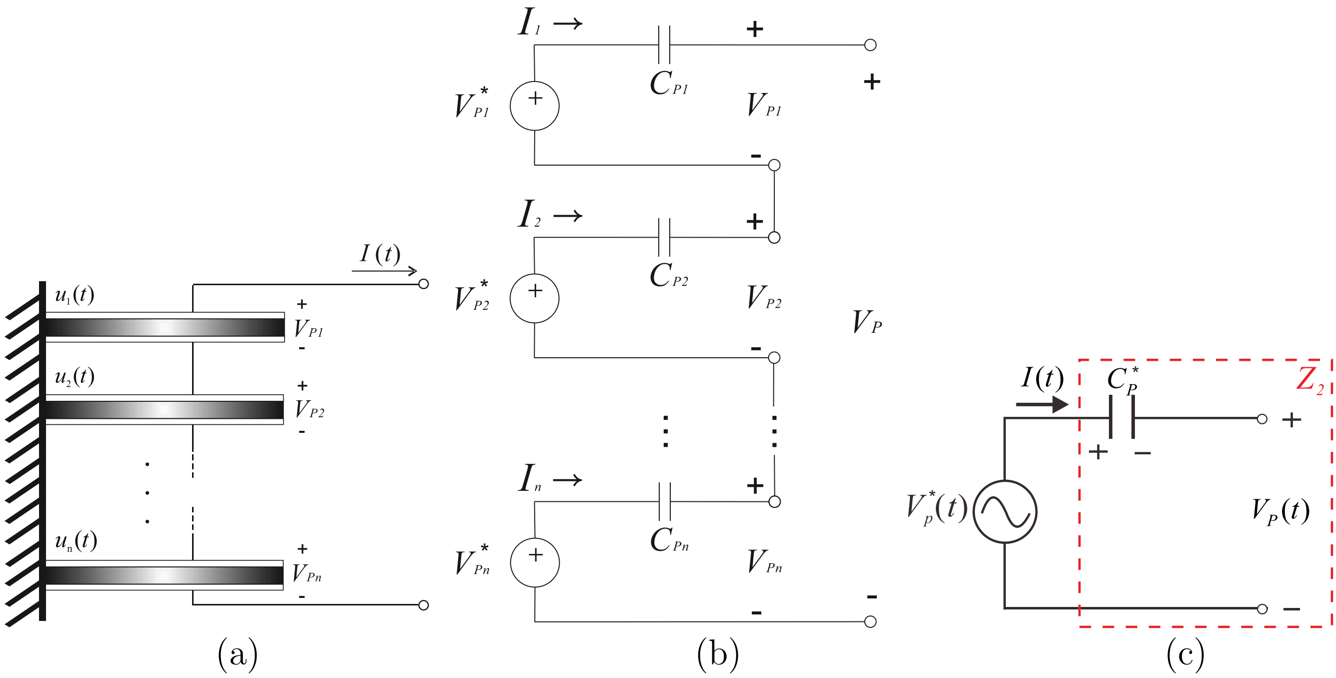

Figure 8. (a) An array of piezoelectric oscillators connected in series. (b) The equivalent voltage model of series connection of piezoelectric oscillators. (c) The overall equivalent voltage model of series connection of piezoelectric oscillators.

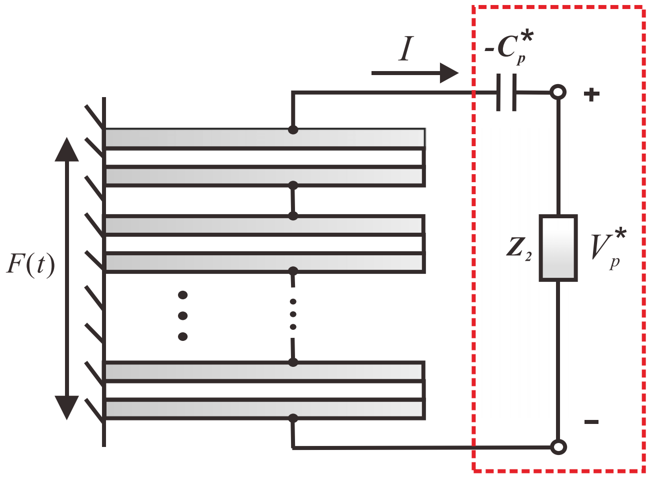

Figure 9. The schematic interpretation of the finite element model of the voltage type for the series connection of piezoelectric oscillators.

Table 1. Geometric properties of a piezoelectric bimorph.

substrate (Cu)	40 mm × 10 mm × 0.1 mm
piezoelectric patch (PZT-5H)	40 mm × 10 mm × 0.2 mm

Table 2. Material constants of Cu and PZT-5H.

Substrate material : Cu	
Density, ρ [kg m^{-3}]	8580
Young's modulus, E [GPa]	120
Poisson's ratio, ν	0.35
Piezoelectric material : PZT-5H	
Density, ρ [kg m^{-3}]	7500
Relative dielectric constant	
$\epsilon_{11}^S/\epsilon_0$	1704.4
$\epsilon_{33}^S/\epsilon_0$	1433.6
Piezoelectric constant [C m^{-2}]	
e_{31}	−6.62
e_{33}	23.24
e_{15}	17.03
Elastic constant [GPa]	
C_{11}	127.2
C_{12}	80.2
C_{13}	84.7
C_{33}	117.4
C_{44}	23.0

4.2. Simulations of dissimilar oscillators

The proposed finite element models offer several advantages of designing electrically rectified piezoelectric energy harvester devices consisting of dissimilar oscillators. Indeed, connected multiple piezoelectric oscillators have been used for enhancing harvested power or for improving bandwidth [2, 4, 11, 28, 31, 34, 64].

Consider the first case where three connected piezoelectric bimorphs are attached to the standard interface circuit. If all the bimorphs are identical, harvested power is expected to be three times larger than that of a single bimorph. However, power reduction arises due to deviations in sizes and materials, and this example shows how the fabrication errors affect it. The geometric and material properties used for the first bimorph are chosen to be the same as those in table 1 and table 2, and therefore, from table 3 the system falls in the range of strong electromechanical coupling. However, it is assumed that there are ± 1 deviations in length for the second

Table 3. Equivalent system parameters.

M (kg)	η_m (N·sec/m)	K (N/m)	Θ (N/V)	C_p (nF)	F_0 (N)	k_e^2	ζ_m
3.8×10^{-4}	4.7×10^{-3}	314	8.4×10^{-4}	26	0.0012	0.0864	0.0068

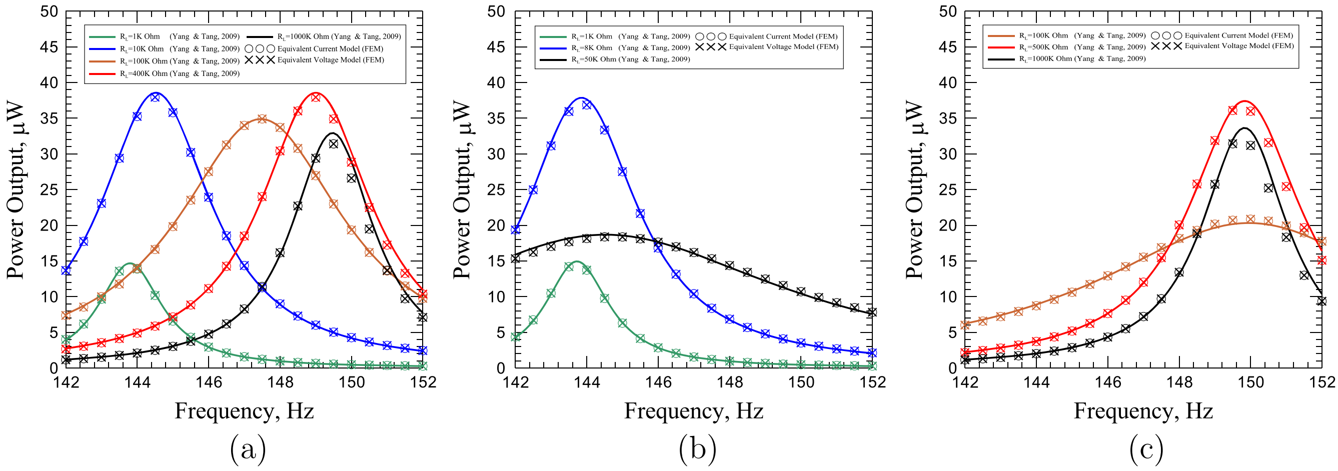

Figure 10. Numerical validation of the present finite element model compared to that based on [67]. Harvested power is against frequency for various resistive loads in the case of the standard interface as in (a), the parallel-SSHI interface as in (b) and the series-SSHI interface as in (c).

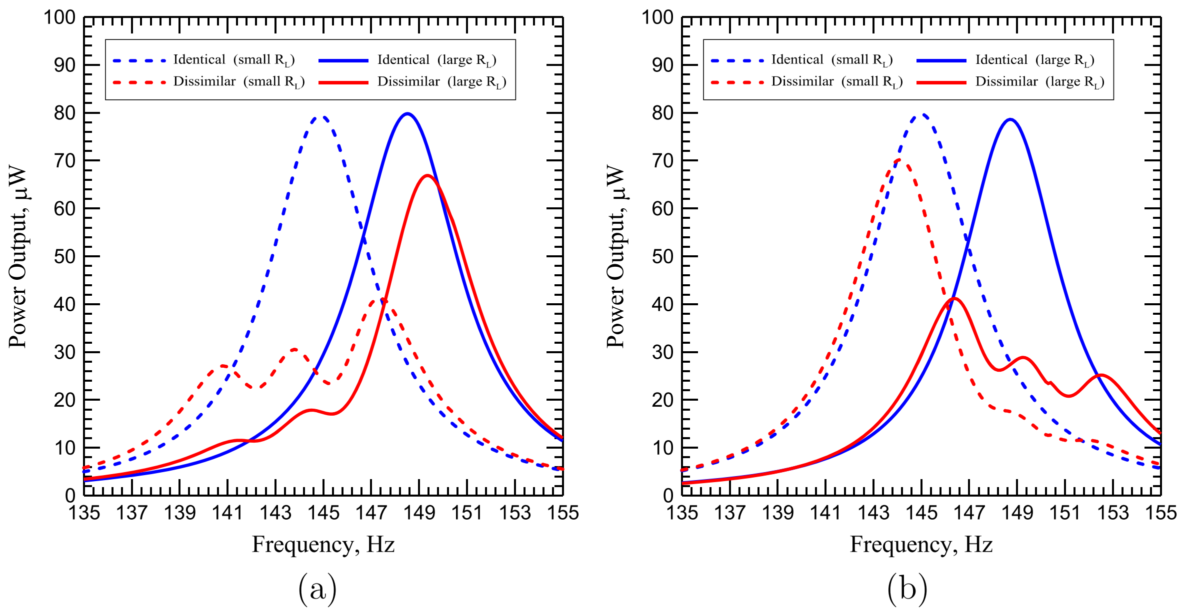

Figure 11. Investigation of power reduction due to fabrication deviations in geometric and material properties. Harvested power is against frequency evaluated at around the optimal load for the device with strong electromechanical coupling. (a) Parallel connection and (b) series connection of three oscillators.

and third bimorphs. In addition, there are ±10% deviations in piezoelectric and permittivity constants for the second and third bimorphs when compared to the first bimorph.

Under the harmonic excitation with 2 m s^{-2} acceleration, harvested power against frequency evaluated around the optimal load is shown in figure 11(a) for the parallel connection of oscillators and in figure 11(b) for the series connection of oscillators. The blue curves refer to the case without deviations in geometric and material properties, while the red curves refer to the case allowing deviations in parameters. For the case of identical bimorphs, figure 10(a) has indicated that a strongly coupled system has two identical peaks in harvested power (see the continuous and dashed blue lines in figure 11). But at the first thought, power reduction would be significant due to large deviation (10%) in piezoelectric material properties. Remarkably, the present finite

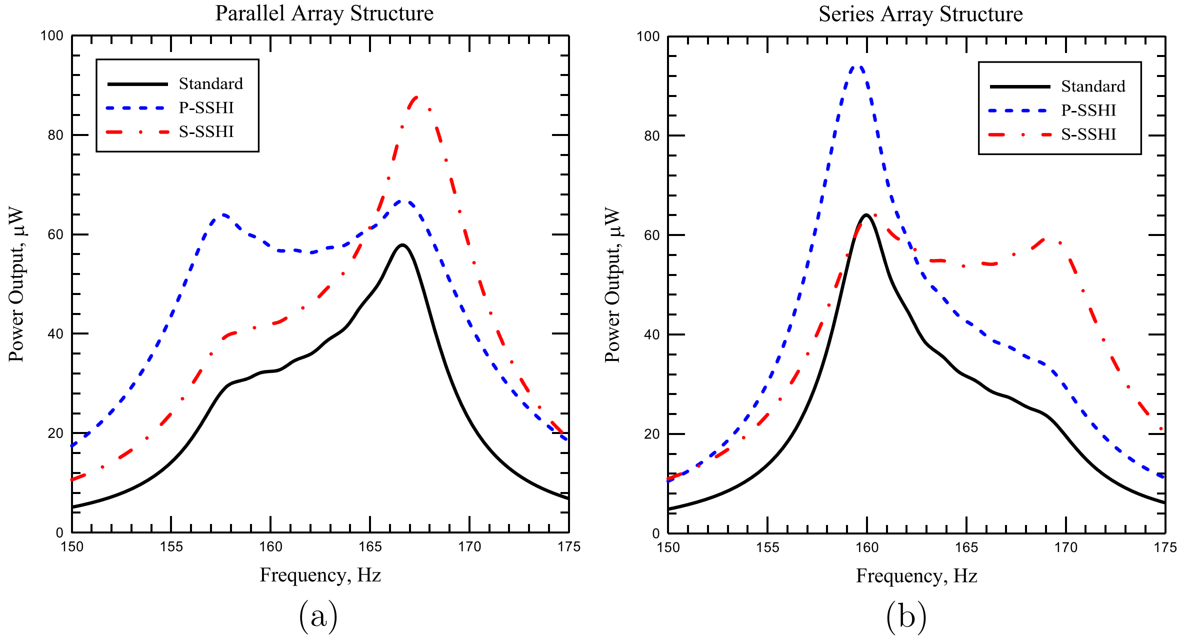

Figure 12. Harvested power is against frequency evaluated at around the optimal load for the device attached to the standard (black), parallel-SSHI (blue) and series-SSHI (red) interface circuits. (a) Parallel connection and (b) series connection of oscillators.

Table 4. Geometric properties of a piezoelectric bimorph and the magnitude of attached proof mass.

substrate (Cu)	40 mm × 10 mm × 0.4 mm
piezoelectric patch (PZT-5H)	40 mm × 10 mm × 0.05 mm
proof mass	0.002 g, 0.011 g, 0.020 g, 0.029 g, 0.038 g, 0.047 g

simulations reveal that power reduction turns out to be small if the operating condition is carefully chosen. For example, from figure 11, the one with large (small) optimal load should be chosen to avoid significant power reduction in the case of parallel (series) connection of oscillators. This gives an important guideline for designing an array system with ability in power boosting.

The second model example is to design a wideband energy harvester device. For example, consider a device consisting of six identical piezoelectric bimorphs. But the resonance is slightly adjusted by attaching different magnitudes of proof mass. The geometric properties of a piezoelectric bimorph and the magnitude of attached proof mass are provided in table 4 with material constants listed in table 2. The device is attached to the different interface circuit, including the standard/parallel-SSHI/series-SSHI interfaces (the electric inversion quality factor $q_I = 0.7$ for the SSHI systems). Under the harmonic excitation with 2 m s^{-2} acceleration, harvested power against frequency evaluated around the optimal load is shown in figure 12(a) for the parallel connection of oscillators and in figure 12(b) for the series connection of oscillators. The different color lines refer to the cases connected to various interfaces. From figure 12(a), the present finite element simulations reveal significant broadband for the parallel connection of oscillators attached to the parallel-SSHI interface. On the other hand, figure 12(b) indicates the use of series-SSHI interface for wideband improvement when the oscillators are connected in series. This gives further guidelines for designing wideband energy harvester devices.

5. Conclusion

This article develops several finite element models suitable for the direct system-level design of electrically rectified piezoelectric energy harvesters. It is based on the proposed equivalent load impedance Z_1 and Z_2 derived from the equivalent current and voltage models. The common energy harvesting circuit with the standard/parallel-SSHI/series-SSHI interface is replaced with the load impedance Z_1 (Z_2) in parallel (in series) to the piezoelectric capacitance of negative value. It follows that the proposed framework is capable of being implemented into conventional finite element solvers, and therefore, provides a useful tool for performance evaluation without resorting to circuit simulators. Another advantage of the proposed framework is the easy extension to the case of multiple piezoelectric oscillators. It is demonstrated that the finite element model of the current (voltage) type is extendable to the case of the parallel (series) connection of oscillators.

The validation is carried out numerically by comparison to the two-step finite element approach by Yang and Tang [67]. Figure 10 shows good agreement for various interface circuits. The framework is then applied to the design of energy harvesting devices with ability either in power enhancement or broadband improvement. The first case discusses how harvested power is reduced due to inevitable fabrication deviations in geometric and material properties of each cantilever bimorph. Remarkably, figure 11 reveals that the reduction in peak power turns out to be small if the large (small) optimal load is carefully chosen for the parallel (series) connection of bimorphs. The second design demonstrates how broadband energy harvesting is achieved by developing array systems with suitable interface circuits. Figure 12 exhibits significant broadband for the parallel (series) connection of oscillators endowed with the parallel-SSHI (series-SSHI) circuit technique.

Acknowledgments

The support from National Taiwan University and from Ministry of Science and Technology under Grant No. 102-2221-E-002-126-MY3 is appreciated.

References

[1] Abdelkefi A, Barsallo N, Tang L, Yang Y and Hajj M R 2014 Modeling, validation, and performance of low-frequency piezoelectric energy harvesters *J. Intell. Mater. Syst. Struct.* **25** 1429–44

[2] Al-Ashtari W, Hunstig M, Hemsel T and Sextro W 2013 Enhanced energy harvesting using multiple piezoelectric elements: theory and experiments *Sensors Actuators* A **200** 138–46

[3] Badel A, Benayad A, Lefeuvre E, Lebrun L, Richard C and Guyomar D 2006 Single crystals and nonlinear process for outstanding vibration-powered electrical generators *IEEE Trans. Ultrason. Ferroelectr. Freq. Control* **53** 673–84

[4] Castagnetti D 2013 A wideband fractal-inspired piezoelectric energy converter: design, simulation and experimental characterization *Smart Mater. Struct.* **22** 094024

[5] Challa V R, Prasad M G and Fisher F T 2011 Towards an autonomous self-tuning vibration energy harvesting device for wireless sensor network applications *Smart Mater. Struct.* **20** 025004

[6] Cottone F, Vocca H and Gammaitoni L 2009 Nonlinear energy harvesting *Phys. Rev. Lett.* **102** 080601

[7] Elvin N G and Elvin A A 2009 A coupled finite element circuit simulation model for analyzing piezoelectric energy generators *J. Intell. Mater. Syst. Struct.* **20** 587–95

[8] Erturk A and Inman D J 2008 Issues in mathematical modeling of piezoelectric energy harvesters *Smart Mater. Struct.* **17** 065016

[9] Erturk A and Inman D J 2011 *Piezoelectric Energy Harvesting* (Chichester: Wiley) doi:10.1002/9781119991151

[10] Erturk A, Renno J M and Inman D J 2009 Modeling of piezoelectric energy harvesting from an L-shaped beam-mass structure with an application to UAVs *J. Intell. Mater. Syst. Struct.* **20** 529–44

[11] Ferrari M, Ferrari V, Guizzetti M, Marioli D and Taroni A 2008 Piezoelectric multifrequency energy converter for power harvesting in autonomous microsystems *Sensors Actuators* A **142** 329–35

[12] Guyomar D, Badel A, Lefeuvre E and Richard C 2005 Toward energy harvesting using active materials and conversion improvement by nonlinear processing *IEEE Trans. Ultrason. Ferroelectr. Freq. Control* **52** 584–95

[13] Hsieh P H, Chen C H and Chen H C 2015 Improving the scavenged power of nonlinear piezoelectric energy harvesting interface at off-resonance by introducing switching delay *IEEE Trans. Power Electron.* **30** 3142–55

[14] Hu Y T, Xue H and Hu H P 2007 A piezoelectric power harvester with adjustable frequency through axial preloads *Smart Mater. Struct.* **16** 1961–6

[15] Jeon Y B, Sood R, Jeong J H and Kim S G 2005 MEMS power generator with transverse mode thin film PZT *Sensors Actuators* A **122** 16–22

[16] de Marqu Jr C, Erturk A and Inman D J 2009 An electromechanical finite element model for piezoelectric energy harvester plates *J. Sound Vib.* **327** 9–25

[17] Karami M A and Inman D J 2011 Electromechanical modeling of the low-frequency zigzag micro-energy harvester *J. Intell. Mater. Syst. Struct.* **22** 271–82

[18] Karami M A, Bilgen O, Inman D J and Friswell M I 2011 Experimental and analytical parametric study of single-crystal unimorph beams for vibration energy harvesting *IEEE Trans. Ultrason. Ferroelectr. Freq. Control* **58** 1508–20

[19] Kauffman J L and Lesieutre G A 2009 A low-order model for the design of piezoelectric energy harvesting devices *J. Intell. Mater. Syst. Struct.* **20** 495–504

[20] Kim J E 2014 Dedicated algorithm and software for the integrated analysis of AC and DC electrical outputs of piezoelectric vibration energy harvesters *J. Mech. Sci. Technol.* **28** 4027–36

[21] Kim J E and Kim Y Y 2011 Analysis of piezoelectric energy harvesters of a moderate aspect ratio with a distributed tip mass *J. Vib. Acoust.* **133** 041010

[22] Lallart M, Anton S R and Inman D J 2010 Frequency self-tuning scheme for broadband vibration energy harvesting *J. Intell. Mater. Syst. Struct.* **21** 897–906

[23] Lallart M and Guyomar D 2008 An optimized self-powered switching circuit for non-linear energy harvesting with low voltage output *Smart Mater. Struct.* **17** 035030

[24] Lee B S, Lin S C and Wu W J Fabrication and evaluation of a MEMS piezoelectric bimorph generator for vibration energy harvesting *J. Mech.* **26** 493–9

[25] Leland E S and Wright P K 2006 Resonance tuning of piezoelectric vibration energy scavenging generators using compressive axial preload *Smart Mater. Struct.* **15** 1413–20

[26] Liang J R and Liao W H 2012 Impedance modeling and analysis for piezoelectric energy harvesting systems *IEEE/ASME Trans. Mechatronics* **17** 1145–57

[27] Liang J R and Liao W H 2012 Improved design and analysis of self-powered synchronized switch interface circuit for piezoelectric energy harvesting systems *IEEE Trans. Ind. Electron.* **59** 1950–60

[28] Lien I C and Shu Y C 2012 Array of piezoelectric energy harvesting by equivalent impedance approach *Smart Mater. Struct.* **21** 082001

[29] Lien I C and Shu Y C 2013 Piezoelectric array of oscillators with respective electrical rectification *Proc. SPIE: Active and Passive Smart Structures and Integrated Systems* ed H A Sodano p. 868806

[30] Lien I C, Shu Y C, Wu W J, Shiu S M and Lin H C 2010 Revisit of series-SSHI with comparisons to other interfacing

circuits in piezoelectric energy harvesting *Smart Mater. Struct.* **19** 125009
[31] Lin H C, Wu P H, Lien I C and Shu Y C 2013 Analysis of an array of piezoelectric energy harvesters connected in series *Smart Mater. Struct.* **22** 094026
[32] Lin S C and Wu W J 2013 Piezoelectric micro energy harvesters based on stainless-steel substrates *Smart Mater. Struct.* **22** 045016
[33] Liu Y, Tian G, Wang Y, Lin J, Zhang Q and Hofmann H F 2009 Active piezoelectric energy harvesting: general principle and experimental demonstration *J. Intell. Mater. Syst. Struct.* **20** 575–85
[34] Lumentut M F, Francis L A and Howard I M 2012 Analytical techniques for broadband multielectromechanical piezoelectric bimorph beams with multifrequency power harvesting *IEEE Trans. Ultrason. Ferroelectr. Freq. Control* **59** 2555–68
[35] Lumentut M F and Howard I M 2014 Electromechanical finite element modelling for dynamic analysis of a cantilevered piezoelectric energy harvester with tip mass offsand under base excitations *Smart Mater. Struct.* **23** 095037
[36] Mathers A, Moon K S and Yi J 2009 A vibration-based PMN-PT energy harvester *IEEE Sensors J.* **9** 731–9
[37] Mo C, Radziemski L J and Clark W W 2010 Analysis of piezoelectric circular diaphragm energy harvesters for use in a pressure fluctuating system *Smart Mater. Struct.* **19** 025016
[38] Moon J W, Jung H J, Baek K H, Song D, Kim S B, Kim J H and Sung T H 2014 Optimal design and application of a piezoelectric energy harvesting system using multiple piezoelectric modules *J. Electroceram.* **32** 396–403
[39] Morris D J, Youngsman J M, Anderson M J and Bahr D F 2008 A resonant frequency tunable, extensional mode piezoelectric vibration harvesting mechanism *Smart Mater. Struct.* **17** 065021
[40] Niri E D and Salamone S 2012 A passively tunable mechanism for a dual bimorph energy harvester with variable tip stiffness and axial load *Smart Mater. Struct.* **21** 125025
[41] Oh S R, Wong T C, Tan C Y, Yao K and Tay F E 2014 Fabrication of piezoelectric polymer multilayers on flexible substrates for energy harvesting *Smart Mater. Struct.* **23** 015013
[42] Ottman G K, Hofmann H F, Bhatt A C and Lesieutre G A 2002 Adaptive piezoelectric energy harvesting circuit for wireless remote power supply *IEEE Trans. Power Electron.* **17** 669–76
[43] Priya S 2005 Modeling of electric energy harvesting using piezoelectric windmill *Appl. Phys. Lett.* **87** 184101
[44] Qin Y, Wang X and Wang Z L 2008 Microfibre-nanowire hybrid structure for energy scavenging *Nature* **451** 809–13
[45] Roundy S and Wright P K 2004 A piezoelectric vibration based generator for wireless electronics *Smart Mater. Struct.* **13** 1131–42
[46] Roundy S, Wright P K and Rabaey J M 2004 *Energy Scavenging for Wireless Sensor Networks with Special Focus on Vibrations* (Boston: Kluwer Academic) doi:10.1007/978-1-4615-0485-6
[47] Rupp C J, Evgrafov A, Maute K and Dunn M L 2009 Design of piezoelectric energy harvesting systems: a topology optimization approach based on multilayer plates and shells *J. Intell. Mater. Syst. Struct.* **20** 1923–39
[48] Schoeftner J and Buchberger G 2013 A contribution on the optimal design of a vibrating cantilever in a power harvesting application—optimization of piezoelectric layer distributions in combination with advanced harvesting circuits *Eng. Struct.* **53** 92–101
[49] Scruggs J T 2009 An optimal stochastic control theory for distributed energy harvesting networks *J. Sound Vib.* **320** 707–25
[50] Seuaciuc-Osorio T and Daqaq M F 2009 On the reduced-order modeling of energy harvesters *J. Intell. Mater. Syst. Struct.* **20** 2003–16
[51] Shahruz S M 2006 Design of mechanical band-pass filters with large frequency bands for energy scavenging *Mechatronics* **16** 523–31
[52] Shu Y C and Lien I C 2006 Analysis of power output for piezoelectric energy harvesting systems *Smart Mater. Struct.* **15** 1499–512
[53] Shu Y C and Lien I C 2006 Efficiency of energy conversion for a piezoelectric power harvesting system *J. Micromech. Microeng.* **16** 2429–38
[54] Shu Y C, Lien I C and Wu W J 2007 An improved analysis of the SSHI interface in piezoelectric energy harvesting *Smart Mater. Struct.* **16** 2253–64
[55] Sodano H A, Inman D J and Park G 2004 A review of power harvesting from vibration using piezoelectric materials *Shock Vib. Dig.* **36** 197–205
[56] Song H J, Choi Y T, Purekar A S and Wereley N M 2009 Performance evaluation of multi-tier energy harvesters using macro-fiber composite patches *J. Intell. Mater. Syst. Struct.* **20** 2077–88
[57] Wang H, Tang L, Shan X, Xie T and Yang Y 2014 Modeling and performance evaluation of a piezoelectric energy harvester with segmented electrodes *Smart Struct. Syst.* **14** 247–66
[58] Wang Q and Wu N 2012 Optimal design of a piezoelectric coupled beam for power harvesting *Smart Mater. Struct.* **21** 085013
[59] Wang W, Huang R J, Huang C J and Li L F 2014 Energy harvester array using piezoelectric circular diaphragm for rail vibration *Acta Mech. Sin.* **30** 884–8
[60] Wickenheiser A M and Garcia E 2010 Power optimization of vibration energy harvesters utilizing passive and active circuits *J. Intell. Mater. Syst. Struct.* **21** 1343–61
[61] Wischke M, Masur M, Goldschmidtboeing F and Woias P 2010 Electromagnetic vibration harvester with piezoelectrically tunable resonance frequency *J. Micromech. Microeng.* **20** 035025
[62] Wu W J, Wickenheiser A M, Reissman T and Garcia E 2009 Modeling and experimental verification of synchronized discharging techniques for boosting power harvesting from piezoelectric transducers *Smart Mater. Struct.* **18** 055012
[63] Xia H and Chen R 2014 Design and analysis of a scalable harvesting interface for multi-source piezoelectric energy harvesting *Sensors Actuators* A **218** 33–40
[64] Xiao Z, Yang T Q, Dong Y and Wang X C 2014 Energy harvester array using piezoelectric circular diaphragm for broadband vibration *Appl. Phys. Lett.* **104** 223904
[65] Xiong X and Oyadiji S O 2014 Modal electromechanical optimization of cantilevered piezoelectric vibration energy harvesters by geometric variation *J. Intell. Mater. Syst. Struct.* **25** 1177–95
[66] Xue H, Hu Y T and Wang Q M 2008 Broadband piezoelectric energy harvesting devices using multiple bimorphs with different operating frequencies *IEEE Trans. Ultrason. Ferroelectr. Freq. Control* **55** 2104–8
[67] Yang Y and Tang L 2009 Equivalent circuit modeling of piezoelectric energy harvesters *J. Intell. Mater. Syst. Struct.* **20** 2223–35
[68] Yang Z and Yang J 2009 Connected vibrating piezoelectric bimorph beams as a wide-band piezoelectric power harvester *J. Intell. Mater. Syst. Struct.* **20** 569–74
[69] Yen T T, Hirasawa T, Wright P K, Pisano A P and Lin L 2011 Corrugated aluminum nitride energy harvesters for high energy conversion effectiveness *J. Micromech. Microeng.* **21** 085037

[70] Zhou W, Penamalli G R and Zuo L 2012 An efficient vibration energy harvester with a multi-mode dynamic magnifier *Smart Mater. Struct.* **21** 015014

[71] Zhu M, Worthington E and Njuguna J 2009 Analyses of power output of piezoelectric energy-harvesting devices directly connected to a load resistor using a coupled piezoelectric-circuit finite element method *IEEE Trans. Ultrason. Ferroelectr. Freq. Control* **56** 1309–18

[72] Zhu M, Worthington E and Tiwari A 2010 Design study of piezoelectric energy-harvesting devices for generation of higher electrical power using a coupled piezoelectric-circuit finite element method *IEEE Trans. Ultrason. Ferroelectr. Freq. Control* **57** 427–37